

Electronegativity and entropy design of layered oxides for sodium-ion batteries

Received: 8 April 2025

Accepted: 15 December 2025

Published online: 08 January 2026

Check for updates

Lu Gan^{1,2,3}, Hu-Rong Yao^{1,4}✉, Jingwen Dai⁵, Zefeng Lai⁴, Xin-Guang Yuan^{1,2}, Wei-Huan He², Qi-lin Zheng¹, Min Wen¹, Wei-Wei Yuan¹, Min Lin⁴, Jian-Mao Xiao⁴, Ze Yu⁴, Yu-Jie Guo², Jinling Liu⁶, Fanghua Ning⁵, Fei Zhan⁷, Denglong Chen⁶, Lituo Zheng¹, Zhigao Huang¹, Chuying OuYang^{4,8}✉ & Yu-Guo Guo^{2,3}✉

Exploring sodium-ion layered oxides with broad compositional diversity is an important approach for the development of high-performance positive electrodes. Structural chemistry determined by composition plays a decisive role in performance improvement, but the relationship between composition and structure becomes more elusive in complex multi-component systems. Here we propose an electronegativity entropy weight concept to understand entropy-dominated phases formation. Electronegativity and configurational entropy are used to quantify key interactions in layered materials. Guided by this understanding, we design a sodium-deficient layered oxide with an O3 stacking sequence. This material demonstrates good structural and thermal stability, along with air stability (negligible performance degradation after air exposure), cycling stability (93.02% capacity retention after 200 cycles), and rate capability (retaining 69.1% capacity retention from 86.5 mA g⁻¹ to 1.73 A g⁻¹). Even in potassium-ion batteries with larger inserted ions, the material still exhibits cycling stability. This strategy provides valuable compositional guidance for the rational design of high-performance layered oxide materials.

Sodium-ion batteries (SIBs) have shown significant potential as an alternative to lithium-ion batteries, especially for applications in the field of large-scale energy storage due to the abundance and cost advantage of sodium resources^{1,2}. Many efforts have been made to develop high-performance positive electrode materials toward realizing high-performance SIBs³⁻⁵. Among various positive electrodes, the layered transition metal oxides Na_xTMO₂ (TM refers to transition metals, such as Ni, Co, Fe, Mn, etc.) are considered as one of the

promising candidates owing to their high theoretical capacities, tunable operating voltage, and ease of synthesis⁶. Most Na_xTMO₂ can be classified into P2- and O3-type structures according to the local Na coordination environment and the oxygen stacking sequence, and the corresponding structure diagram is displayed in Supplementary Fig. 1⁷. Generally, Na_xTMO₂ with a high Na content (x > 0.80) tends to form an O3-type structure with narrow octahedral Na⁺ sites, originating from the strong shielding effect of positively charged Na⁺ in the adjacent

¹Fujian Provincial Key Laboratory of Quantum Manipulation and New Energy Materials, College of Physics and Energy, Fujian Normal University, Fuzhou, China.

²CAS Key Laboratory of Molecular Nanostructure and Nanotechnology, CAS Research/Education Centre for Excellence in Molecular Sciences, Beijing National Laboratory for Molecular Sciences (BNLMS), Institute of Chemistry, Chinese Academy of Sciences, Beijing, China. ³School of Chemical Sciences, University of Chinese Academy of Sciences, Beijing, China. ⁴Fujian Science and Technology Innovation Laboratory for Energy Devices (21C-Lab), Contemporary Ampere Technology Co., Limited (CATL), Ningde, China. ⁵Institute for Sustainable Energy, College of Sciences, Shanghai University, Shanghai, China. ⁶College of Environmental and Resource Sciences and College of Carbon Neutral Modern Industry, Fujian Normal University, Fuzhou, China. ⁷Beijing Synchrotron Radiation Facility, Institute of High Energy Physics, Chinese Academy of Sciences, Beijing, China. ⁸Department of Physics, Laboratory of Computational Materials Physics, Jiangxi Normal University, Nanchang, China. ✉e-mail: yaoyao@fjnu.edu.cn; cyouyang@jxnu.edu.cn; ygguo@iccas.ac.cn

TMO₂ slabs⁸. Similarly, the P2 structure with open prismatic paths is commonly found in low Na compounds due to the dominant role of electrostatic repulsive forces in low sodium systems⁹. Although the sodium content has a significant impact on the stacking structure, the phase formation is complex and subject to various factors^{10,11}. Hu et al. proposed a recent strategy using cation potentials to modulate TMO₂ interslab interaction, contributing to the possibility of predicting stacked structures¹². For a constant Na content, the TM component with a larger cationic potential (namely, the higher oxidation state or a smaller ionic radius) leads to stronger electrostatic cohesion forces between TM–O with a small $d_{(O-TM-O)}$, thus contributing to a weakened Na–O interaction and open prismatic Na sites of P2 stacking structure. The anomalous P2-type Na_{5/6}Li_{5/18}Mn_{13/18}O₂ materials with high Na content were synthesized based on this designing principle. Comparatively, the O3-type oxide with low Na content is rarely reported, mainly because the cationic potential of most TM elements (Ni, Fe, Co, Mn, etc.) do not conform to the unusual small rules (Supplementary Table 1)¹³. In addition, for high-entropy systems, the relationship between composition and structure becomes more elusive because the cationic potential approach cannot provide a sensible guideline in entropy-dominated phases.

High-entropy oxides, as an expansive concept of high-entropy materials, have gained broad recognition in the battery field due to their characteristic physical and chemical features^{14–16}. Compared with traditional oxides, high-entropy layered oxides consist of five or more elements with a highly disordered transition metal layer^{17–19}. Another definition is derived from the quantification of configurational entropy (S_{config}), which is high-, medium- and low-entropy when $S_{\text{config}} \geq 1.5R$, $1.5R > S_{\text{config}} \geq 1.0R$ and $S_{\text{config}} < 1.0R$ (R is the gas constant $8.314 \text{ J mol}^{-1} \text{ K}^{-1}$), respectively²⁰. The electronic localization interactions caused by electronegativity differences of bonding elements affect structures and properties of high entropy materials^{21,22}. For layered oxides, the electron cloud of oxygen is affected by the TM and Na ions^{23,24}. When the electronegativity of TM increases, its attraction to electrons of oxygen strengthens, causing a localized electronic structure of the transition metal layer²⁵. The enhanced electronic localization also decreased the electron density between Na–O, limiting the electrostatic interaction between electrons and interlayer sodium ions^{26,27}. Moreover, the increase of configurational entropy and the enhanced degree of disorder also perturb the localization degree of electronic structure, thereby affecting the phase stability^{28,29}.

Considering the combined effect of cation-oxygen interactions and configurational entropy, we propose the electronegativity entropy weight (W_{χ}) concept to predict the stacking structure of entropy-dominated materials, using ion electronegativity (IEN) to quantify the relationship between cations and oxygen electron cloud, and configurational entropy (S_{config}) to characterize the extent of the impact of entropic disorder on phase structure. The results show that the weighted value W_{χ} reasonably describes the interlayer interactions in medium- and high-entropy materials. Based on the analysis, we design a low-sodium-content O3 positive electrode. To construct a highly disordered TM configuration, the transition metal components are quantitatively designed for a high electronegativity entropy weight value. The obtained Na_{0.67}Ni_{0.18}Cu_{0.18}Fe_{0.15}Co_{0.15}Mn_{0.17}Ti_{0.17}O₂ (O3-Na0.67, $N=6$) manifests the anticipated O3-type arrangement with significantly reduced sodium content. The practicality of the material is demonstrated by its good thermal stability, air stability, and electrochemical stability. The combination of X-ray absorption spectroscopy (XAS), X-ray photoelectron spectroscopy (XPS), and density functional theory (DFT) calculations reveals the diversity of local structures and the multiplicity of redox centers in the framework, ensuring its good stability. The material exhibits a good capacity retention of 93.02% after 200 cycles in sodium-ion batteries, and 70.24% retention after 100 cycles in potassium-ion batteries, comparing favorably with conventional O3 materials. The research on high-

entropy oxide materials is still in the early exploratory stage. A deeper understanding of the key compositional factors in structural chemistry will help us more rationally design high-performance materials.

Results

The definition of electronegativity originates from the ability of an atom to attract electrons, and the IEN concept is further proposed based on the actual coordination environment of atoms. The IEN values based on oxidation states, spin states, and coordinating cations can be used to qualitatively assess the nature and strength of chemical bonds³⁰. Pauling proposed that the ionic and covalent character of a bond can be expressed by the percentage of ionic character in a single bond, which is determined by the electronegativity difference ($\Delta\chi$) of the bonding atoms³¹. The greater the electronegativity difference between the bonding anion and cation, the higher the percentage of ionic bonding and the smaller the covalent bonding percentage³². The typical Na_xTMO₂ layered structure consists of alternately stacking of edge-sharing TMO₆ octahedral and Na ions layers (Fig. 1a). In the O–TM–O–A–O configuration of the layered oxide, oxygen atoms are simultaneously subjected to Coulombic attraction from the transition metal and alkali metal in opposite directions³³. In the TM–O–A structure, a higher IEN value of TM leads to reduced electronegativity difference $\Delta\chi$ between TM and O, which enhances their orbital overlap and promotes more covalent TM–O bonding with stronger binding and shorter $d_{(O-TM-O)}$ distances. This strengthened TM–O interaction concurrently weakens the Na–O bonding in the same TM–O–A configuration, yielding more open AO₆ structural arrangements with expanded $d_{(O-A-O)}$ spacing (Fig. 1b). Differential charge density analysis on multicomponent TM systems was performed to provide further evidence for the significant influence of electronegativity on electronic structure. As shown in Fig. 1c (details in Supplementary Data 1), TMs with higher electronegativity (e.g., Ni, Cu, Co, $\chi > 1.8$) exhibit greater charge accumulation along TM–O bonds, indicating stronger covalent character. In contrast, TMs with lower electronegativity (e.g., Mn, Ti, $\chi < 1.6$) show more charge transfer to oxygen, reflecting stronger ionic characteristics.

This shift in electron density on TM–O and O–Na bonds is essentially a delocalization/localization phenomenon of electrons on chemical bonds³⁴. Moreover, the degree of disorder introduced by high-entropy components also exerts a significant influence on the stacking structure. The high entropy strategy is usually introduced to construct highly disordered ion arrangements and consequently delocalized electronic structure. The disordered ion arrangements can promote delocalized electronic structures, which results in a weakened interaction between TM and O, and thus a stronger Na–O bonds and a contractive Na layer of O3 structure.

In order to identify a quantitative indicator for the interlayer interactions in layered oxides, we define the electronegativity entropy weight to express the weights of electronegativity and configurational entropy in structure formation:

$$W_{\chi} = \prod \chi_{\text{Cation}} \times \frac{S_{\text{config}}}{R} \times \frac{r_{\text{TM}}}{r_{\text{A}}} \quad (1)$$

Where $\prod \chi_{\text{Cation}}$ represents the cationic electronegativity index, defined as $\prod \chi_{\text{Cation}} = \frac{n_{\text{A}}}{n_{\text{Cation}}} \times \bar{\chi}_{\text{A}} \times \Delta\chi_{\text{TM}}$; $\frac{n_{\text{A}}}{n_{\text{Cation}}}$ is the molar ratio of alkali to total cations, which serves as a quantitative descriptor for attraction O of alkali metal ions; $\bar{\chi}_{\text{A}}$ represents the average electronegativity difference between O and alkali metal in the AO₂ layer. Since the layered oxides crystallize with the coordination number CN = 6, the χ_i value of IEN is chosen as the reference (Supplementary Fig. 2)³⁵; $\Delta\chi_{\text{TM}} = \chi_{\text{O}} - \bar{\chi}_{\text{TM}}$ is the difference in electronegativity between O and the average χ_i of TM ions. $\Delta\chi_{\text{TM}}$ is used to quantify the ionic degree of bond formation between transition metal ions and oxygen, defined as the bond polarity index. $|S_{\text{config}}|$ represents the absolute value of

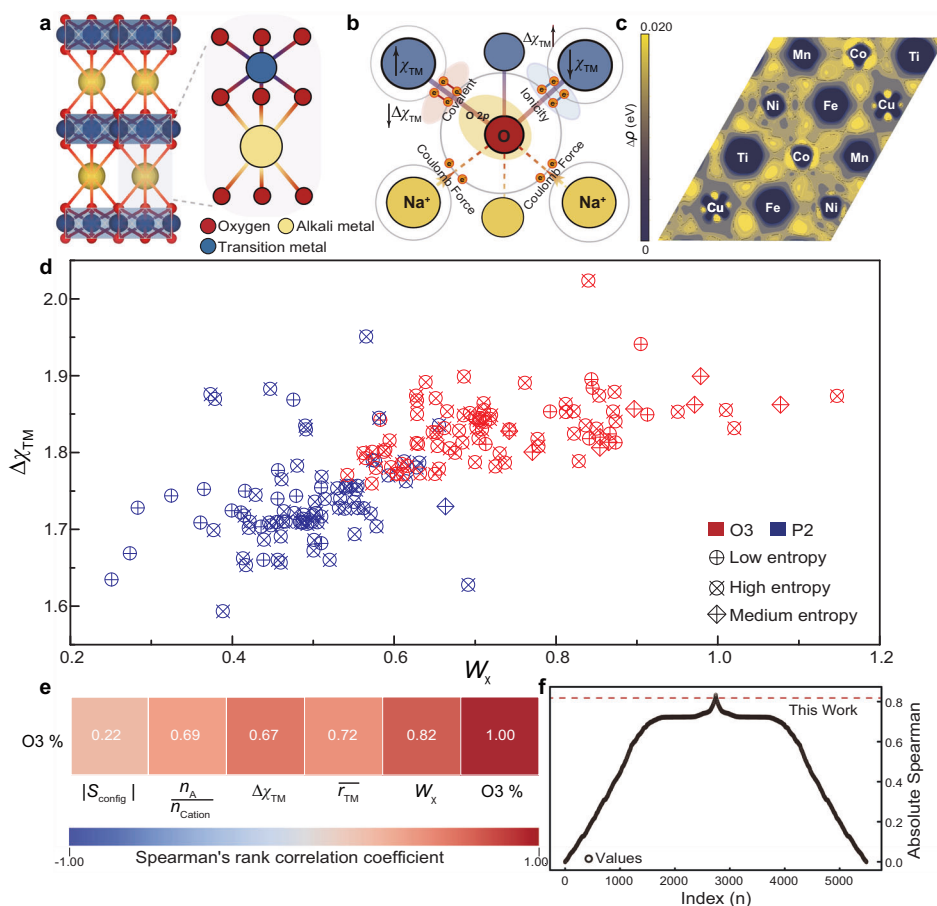


Fig. 1 | Electronegativity entropy weight concept and theoretical validation.

a Stacking layered structure of Na_xTMO_2 . **b** Relationship between cationic electronegativity and anionic electron cloud. **c** The two-dimensional differential charge density maps projected along the (001) plane of $\text{O3-Na}_{0.667}\text{TMO}_2$ (TM: Ni, Cu, Co, Fe, Mn, Ti). The difference charge density ($\Delta\rho$) is defined as $\Delta\rho = \rho(\text{system}) - \rho(\text{atom})$, where $\rho(\text{system})$ denotes the charge density of the

system, and $\rho(\text{atom})$ is the superposition of atomic charge densities calculated by setting ICHARG = 12. The yellow and blue colors, respectively, represent positive and negative iso-surfaces. The value of the iso-surface is 0.02 e/Bohr^3 .

d Relationship between W_x value and $\Delta\chi_{\text{TM}}$ of statistic P2- and O3-type.

e Spearman's rank correlation coefficient heat map of materials with different configurational entropy. **f** Distribution of Absolute Spearman Values.

configurational entropy (Supplementary Equation (2))³⁶. $\frac{r_{\text{TM}}}{r_{\text{A}}}$ is the ratio of the average radius of transition metal to alkali metal ions.

By calculating the W_x values of a series of reported low/high/medium-entropy P2-/O3-type layered oxides (detailed information in Supplementary Tables 2–4), we identified a clear linear relationship between W_x and $\Delta\chi_{\text{TM}}$ values (Fig. 1d). Further data examination revealed that there is a clear distinction in W_x values among different stacking structures. Spearman's rank correlation coefficient (Fig. 1e) reveals a strong positive correlation between W_x and the O3 structure. Components with higher W_x values are more inclined to form the O3 phase, whereas those with lower W_x values favor the formation of the P2 phase. We further performed a comprehensive analysis of basic operations involving the feature variables in the formula by integrating machine learning techniques. Among the 5488 combinations obtained, the current formula demonstrates a prominent correlation of 0.8182 (Fig. 1f). Notably, the analyzed data also include P2-type layered oxides with an anomalous high sodium content, indicating that the sodium concentration is not the sole determinant of the stacking structure. These findings reveal the critical role of the W_x value in describing the interlayer interactions and the Na^+ coordination environment of multicomponent materials. The high W_x values are generally associated with high probabilities of O-type structure formation, and vice versa. The close correlation between W_x and structure provides a theoretical direction for designing advanced materials. To further elucidate the role of configurational entropy, machine learning

approaches were employed for analysis. The influence of entropy on structural properties was found to be negligible in systems where $|S_{\text{config}}| < 1$. However, as $|S_{\text{config}}| \geq 1$, its effect becomes increasingly apparent, exerting a notable impact on the resulting structure (Supplementary Fig. 3). We further investigated the influences of $\Delta\chi_{\text{TM}}$ and $|S_{\text{config}}|$ on W_x to gain a deeper understanding of their impacts on the evolution of stacking structures.

Based on the above understanding, we design a specific material with O3 stacking structure but with traditional P-type sodium content by adjusting $|S_{\text{config}}|$ and $\Delta\chi_{\text{TM}}$ (Fig. 2a). Firstly, the impact of configurational entropy is quantitatively analyzed. We chose six elements (Ni, Mn, Cu, Co, Fe, and Ti) to form the TM components according to the following criteria (Supplementary Table 5): a) the selected TM oxide precursors have different crystal structure and space group, which prevents the obtained system from forming the precursor configuration but instead forming a layered structure different from the oxide precursor³⁷. b) The elements present distinguished valence states and electronic structures in the multicomponent system, thus promoting the realization of high entropy properties. c) The similar ionic radius facilitates an easier complete miscibility in a single phase. A high temperature up to 950°C is set in order to highlight the impact of $|S_{\text{config}}|$. Based on the common oxide with Ni and Mn component $\text{Na}_{0.67}\text{Ni}_{0.33}\text{Mn}_{0.67}\text{O}_2$ (abbreviated as $N=2$), we gradually added Cu, Co, Fe, and Ti into the transition metal layer (abbreviated as $N=3, 4, 5, 6$) and characterized the evolution of crystal structures. As shown in

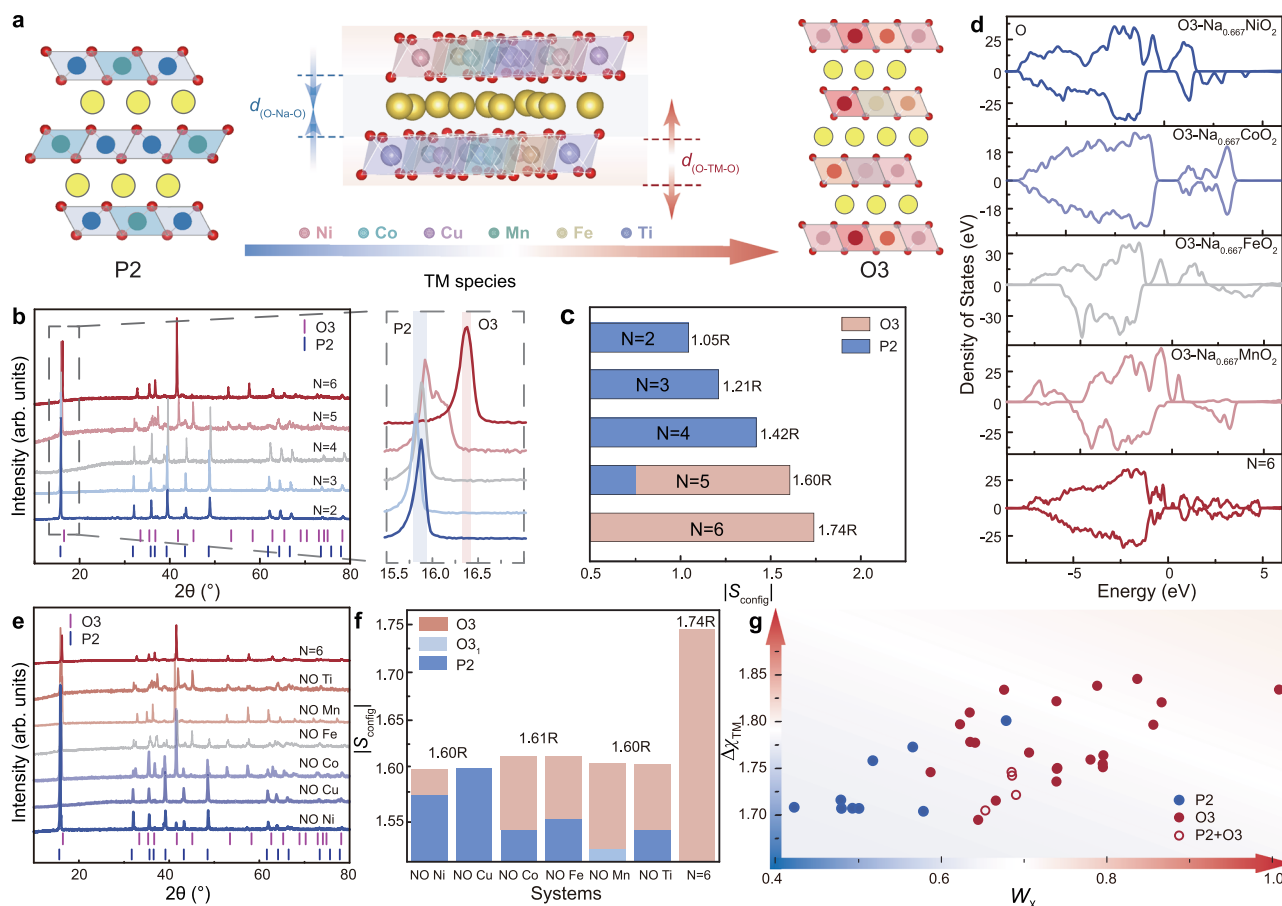


Fig. 2 | The role of configurational entropy in phases. **a** Schematic illustrations of $d_{(\text{O-Na-O})} / d_{(\text{O-TM-O})}$ with TM species increase. **b** XRD patterns of the layered oxide series with an increasing number (N) of transition metal species. N represents the total number of different TM cations in the composition. Standard reference patterns for P2 and O3 phases are included. (P2: ICDD No. 01-070-3726, O3: ICDD

No. 01-073-2048). **c** The change of O/P phase structure with entropy values. **d** The O 2p comparative PDOS of mono-TM and multi-TM ($N = 6$) systems. **e** XRD patterns of a composition series where individual components are removed from the 6 compositions. **f** The change of O/P phase structure with entropy values. **g** Relationship between W_x value and $\Delta\chi_{\text{TM}}$ of synthetic materials.

Fig. 2b, the (002) diffraction peak of P2 phase generally shifts to a higher angle as the increase of transition metal species, reflecting the contraction of the unit cell along the c -axis. The peaks from the O3 phase appear when the TM species is increased to 5 (Supplementary Fig. 4), and the material with 6 TM species shows a pure O3 structure. The $|S_{\text{config}}|$ of the actual synthesized systems ($N = 2, 3, 4, 5, 6$ in Fig. 2c) are 1.05 R, 1.21 R, 1.42 R, 1.60 R, and 1.74 R, respectively. According to the refined crystallographic data summarized in Supplementary Tables 6–10, the components of the P2 phase gradually decrease, accompanied by the increase of the O3 phase with the $|S_{\text{config}}|$ increase, and finally the pure O3 phase is obtained. A comparison of the PDOS of the O 2p orbitals in the multi-component and mono-TM systems (Fig. 2d and Supplementary Fig. 5) further shows broader bandwidths in multi-component TM systems, signifying greater global electron delocalization. These results establish that the high-entropy multi-component system makes the structure more delocalized in the state of disordered ion arrangement. Modulating configuration entropy enables the regulation of electron delocalization/localization, thereby directing the structural evolution of layered oxides. We further study the effect of entropy in structural configuration by regulating the synthesis temperature. The powder sample $N = 6$ with a pure O3 structure was reheated at 750 °C, and the impurity phase appeared (Supplementary Fig. 6). The enthalpy ($\Delta H = T\Delta S$) driven phase segregation occurs at a lower temperature, which proves that configurational entropy plays a decisive role in the solid solution phase structure at high-temperature synthesis conditions. We further confirm the

effect of a high entropy strategy to design an anomalous configuration by increasing the TM species N from 6 to 8 (Supplementary Fig. 7).

We further demonstrate the influence of transition metal cations on phase structure formation. In the $N = 6$ system with one of the TM components removed (abbreviated as No TM in Fig. 2e, f and Supplementary Tables 11–15), no solid solution O3 phase can be synthesized for $|S_{\text{config}}|$ below 1.74 R. It is noteworthy that materials with similar values of $|S_{\text{config}}|$ (1.60 R and 1.61 R) can exhibit different P/O composite phase structures, indicating another key factor, in addition to configurational entropy, affects the stacking structure.

Based on the understanding, we design an anomalous O3 structure with a low Na content of 0.538 (designated as $\text{Na}_{0.538}\text{Ni}_{0.18}\text{Cu}_{0.18}\text{Co}_{0.15}\text{Fe}_{0.15}\text{Mn}_{0.17}\text{Ti}_{0.17}\text{O}_2$ (O3-Na0.538) in Supplementary Fig. 8) by maintaining W_x value above this critical threshold. Inductively coupled plasma-optical emission spectroscopy (ICP-OES) analysis of O3-Na0.538 confirmed the Na content (Supplementary Table 16), a relatively low value for O3-type materials. In addition, we synthesized more medium- and high-entropy materials to explore the factors influencing the structure (Supplementary Fig. 9). We calculated the W_x values for a series of materials based on Eq. (1) and compared them with $\Delta\chi_{\text{TM}}$ as presented in Fig. 2g and Supplementary Tables 17–18. There is a positive correlation observed between W_x and $\Delta\chi_{\text{TM}}$. It is worth noting that the component with a W_x in the range of 0.58–0.71 often exhibits a mixed P/O phase, and slight variations in synthesis conditions can significantly affect phase stability. These findings underscore that the $|S_{\text{config}}|$ and $\Delta\chi_{\text{TM}}$ playing a critical and

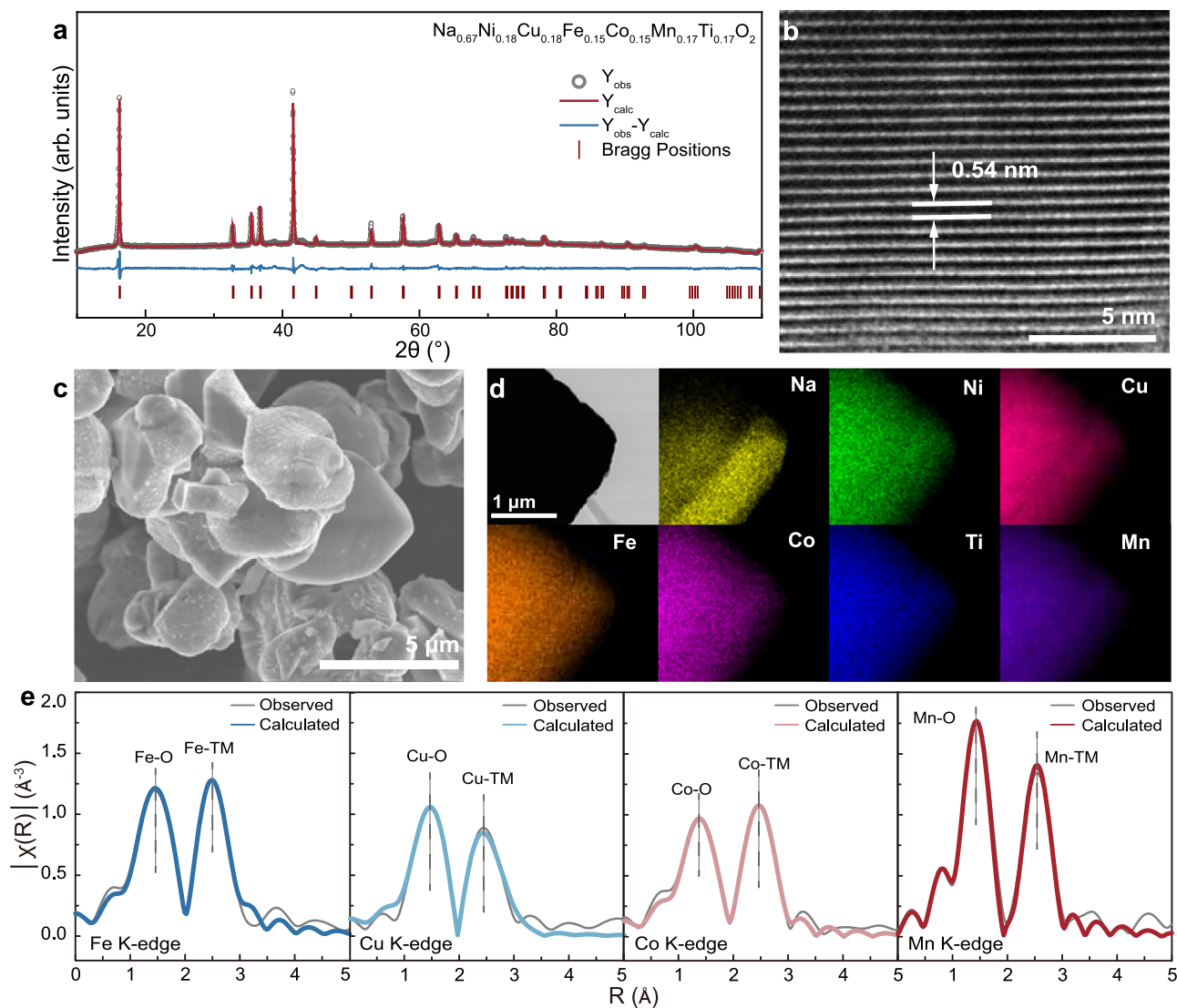


Fig. 3 | Structural and elemental characterization of O3-Na_{0.67}. XRD pattern and Rietveld refinement of **a** O3-Na_{0.67}. **b** TEM images of the O3-Na_{0.67}. **c** SEM images of O3-Na_{0.67}. **d** TEM-EDS mapping results of O3-Na_{0.67}. **e** EXAFS spectra of Fe k-edge, Cu k-edge, Co k-edge and Mn k-edge.

synergistic role in determining the stacking structure of the entropy-driven materials.

High entropy O3-Na_{0.67} is synthesized by a simple solid-state reaction as a studied object and compared with common P2 materials with a normal Na content of 0.67. Supplementary Table 19 displays the ICP-OES result of O3-Na_{0.67}, consistent with our initial design compositions. The X-ray powder diffractometer (XRD) pattern of O3-Na_{0.67} is fully indexed to the O3-type layer structure with a $R\bar{3}m$ space group (Fig. 3a)³⁸. The Rietveld refinement results further indicate its common O3-structure lattice parameters of $a=b=2.955$ Å, $c=16.335$ Å, and 1.555 of $d_{(O-Na-O)}/d_{(O-TM-O)}$ value. All diffraction peaks are well-fitted with a structural model in which six transition metal components are randomly distributed in the TMO₂ slabs. No significant characteristic superstructure peak can be observed, originating from the high entropy component breaking the ordering distribution in the AB -plane. The transmission electron microscope (TEM) image (Fig. 3b) also demonstrates the layered structure with a lattice plane distance of 0.546 nm, corresponding to the (003) plane of the O3 phase. The scanning electron microscope (SEM) image in Fig. 3c shows the bulk samples with a particle size range from 3 to 5 μm. The uniform distribution of various elements is demonstrated by energy dispersive spectroscopy (EDS) mapping (Fig. 3d). The extended X-ray

absorption fine structure spectra (EXAFS) in Fig. 3e provide more information on the local coordination structure, and the corresponding refined bond lengths of TM-O and TM-TM are summarized in Supplementary Table 20. The first shell of Mn-O bond length is about 1.91 Å, while the other bond lengths are higher than 1.95 Å. The bond length between the transition metal and oxygen is susceptible to valence state the higher the valence state the shorter the bond length. The second shell TM-TM bond lengths are almost the same for all elements, which means that the transition metal ions are randomly distributed in TMO₂ with a disordered arrangement^{39,40}. The homogeneous distribution of metal ions results in a more homogeneous redox reaction and reduces the heterogeneity of the composition, resulting in lower stresses and better interparticle stability.

The effect of the random distribution of transition metal ions on the electrochemical performance was also examined by galvanostatic charge/discharge (GCD) tests in Na half-cells. The unmodified P2-Na_{0.67}Ni_{0.33}Mn_{0.67}O₂ (P2-Na_{0.67}) with low entropy component and traditional P2 structure is selected to be the control group. From the XRD patterns in Supplementary Fig. 10, P2-Na_{0.67} contains obvious Na⁺/vacancy ordering in alkali metal layers, indicated from the superlattice peaks at 27.2° and 28.4°⁴¹. The superlattice characteristic is in stark contrast to the highly disordering of high-entropy system

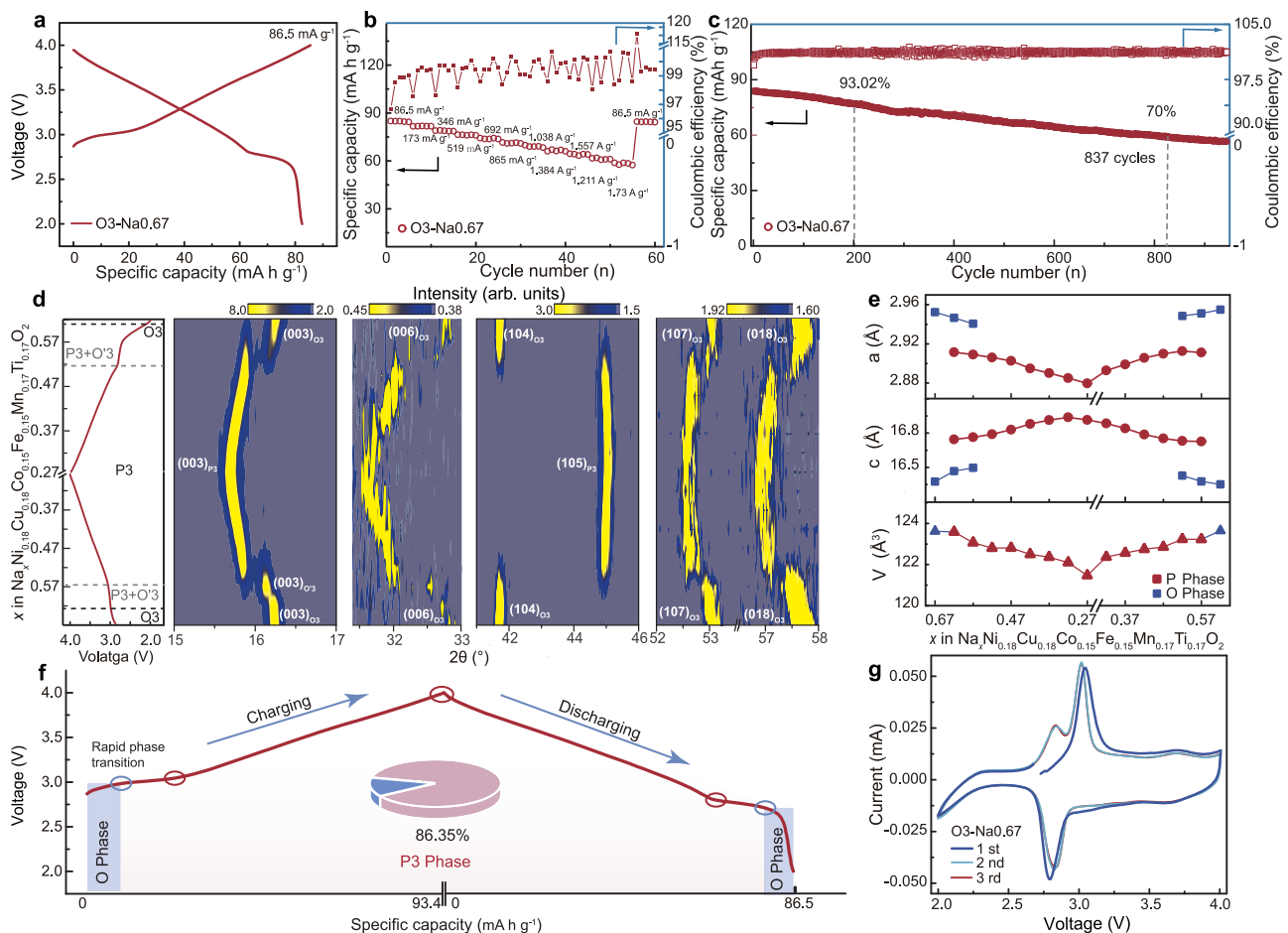


Fig. 4 | Electrochemical performance and structural evolution. **a** GCD curves for the first cycle between 2.0 and 4.0 V, **b** rate performances, **c** cycling performances and coulombic efficiency of O3-Na0.67. **d** in situ XRD patterns of O3-Na0.67 during

the first charge. **e** The *a*, *c* axis, and *V* lattice parameter changes in the as-prepared samples obtained by fitting the in situ XRD data. **f** Schematic diagram of charge-discharge behavior. **g** The first three cyclic voltammetry curves of O3-Na0.67.

discussed above. O3-Na0.67 also shows unusual electrochemical behaviors benefited from the different structure features. Figure 4a displays the GCD curve of the first cycle tested at a current density of 86.5 mA g^{-1} ($1 \text{ C} = 173 \text{ mA h g}^{-1}$) in the voltage range of 2.0–4.0 V. Four improvements of O3-Na0.67 are observed, firstly, 107.7% of initial Coulombic efficiency is achieved instead of the common ~80% in low Na content systems, which is an important indicator for the material practicality^{42–45}. Secondly, O3-Na0.67 displays a smoother charge/discharge curve above 3.3 V, indicating a solid-solution behavior without Na^+ /vacancy superlattice rearrangement, which is different from the multiple plateaus of traditional O3 or P2 materials. Thirdly, O3-Na0.67 affords a better rate performance originating from the highly disordered structure. As shown in Fig. 4b, O3-Na0.67 can deliver a high-capacity retention of 84.2% and 69.1% even cycled at 865 mA g^{-1} and 1.73 A g^{-1} . Lastly, a good cycling stability is obtained with 93.02% capacity retention after 200 cycles at 86.5 mA g^{-1} , which is competitive in the conventional O3 materials with multiphase transition (Supplementary Table 21). Moreover, the O3-Na0.67 can cycle for 837 times with 70% capacity retention (Fig. 4c), and O3-Na0.538 demonstrated good rate and cycle performance (Supplementary Fig. 11).

The in situ XRD measurements during the first electrochemical cycle were executed at 17.3 mA g^{-1} within a voltage range of 2.0–4.0 V to explore the structure evolution upon de-/sodiation (Supplementary Fig. 12). Figure 4d is the contour maps of the main diffraction peaks evolution and corresponding electrochemical curves. When Na^+ is being extracted from the crystal structure, the (003) peak of the O3

phase gradually moves to a lower angle without the appearance of any new peaks, indicating a solid solution reaction with the *c*-axis expansion. Upon further charging, the electrochemical curve exhibits a plateau at approximately 3.0 V, corresponding to the formation of the O'3 phase and an O–P two-phase region. This phase transition is evidenced by a reduction in the intensity and splitting of the (104)_{O3} peak and accompanied by the emergence of P3 phase diffraction peaks⁴⁶. After the complete disappearance of the O phase, material continues to be desodiated with P3 structure until charged to 4.0 V, consistent with a solid solution reaction of the sloping region above 3.0 V. Upon the discharging process, the XRD patterns undergo an opposite evolution, indicating the high reversibility of the O–P phase transition. We further analyzed the variation of lattice parameters and volume of O3-Na0.67 along with Na extraction/insertion. As Fig. 4e shown, the lattice parameters *a*, *c* and volume *V* change by 2.47%, 3.44% and 1.74% upon charged to 4.0 V, respectively. When discharged to 2.0 V, the *a*, *c* and *V* values only varied by 0.088%, 0.154% and 0.021% relative to the original structure. The material undergoes only one rapid phase transition of O–P throughout the charging process, and the P3 phase with a large diffusion channel exists in a high-capacity range of up to 86.35% (Fig. 4f), which results in small volume changes and good structure stability and rate performance. The galvanostatic intermittent titration technique (GITT) measurements were performed to obtain more insight into Na^+ transport during charge/discharge. O3-Na0.67 maintains a Na^+ diffusion coefficient (D_{Na^+}) of 8.2×10^{-12} to $1 \times 10^{-11} \text{ cm}^2 \text{ s}^{-1}$ throughout the plateau, and sloping regions of the charging curve

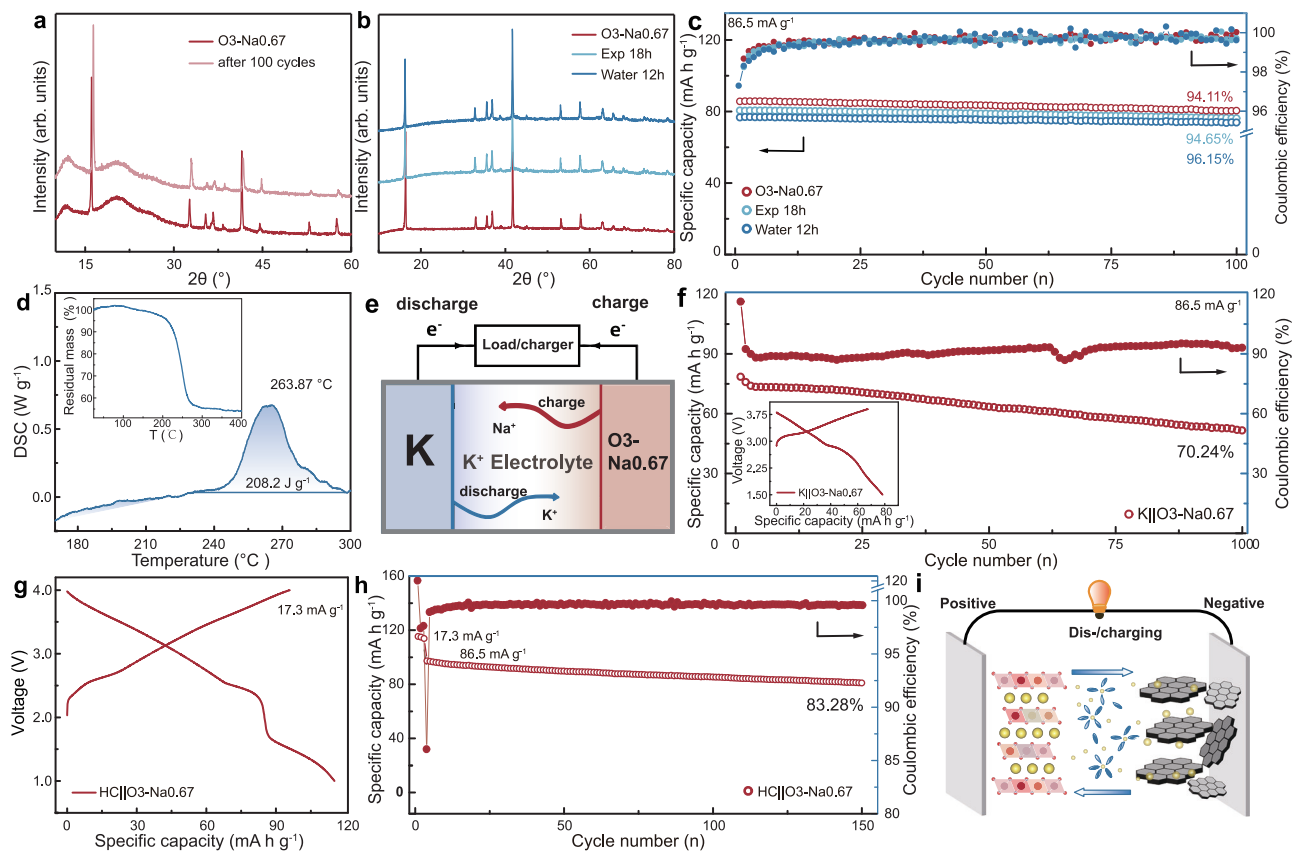


Fig. 5 | Comprehensive stability and practical battery performance. **a** XRD patterns of O3-Na_{0.67} electrode. **b** XRD patterns and **c** cycling performances of fresh and aged O3-Na_{0.67}. **d** DSC profile and thermogravimetric analysis–mass spectrometry (TGA–MS) of O3-Na_{0.67} electrode. The shaded area under the exothermic peak corresponds to the integrated enthalpy change of 208.2 J g⁻¹. The inset shows the corresponding TGA curves, where the residual mass is plotted as a function of temperature. **e** Schematic illustrations of the electrochemical ion-

exchange method. **f** Cycling performance of the O3-Na_{0.67} positive electrode in a K half-cell. The inset shows the galvanostatic charge-discharge profiles for the first cycle in the range of 1.5–3.9 V at 86.5 mA g⁻¹. **g** Initial charge/discharge curves of the full cell of O3-Na_{0.67} positive electrode and hard carbon negative electrode in the range of 1.0–4.0 V at 17.3 mA g⁻¹. **h** Cycling performance with Coulombic efficiency of the full-cell at 86.5 mA g⁻¹, and **i** schematic drawing of the full-cell configuration.

(Supplementary Fig. 13). The gentle fluctuation of D_{Na^+} implies that the O-P phase transition is mild, which is different from traditional O3 materials. Besides, cyclic voltammetry (CV) tests were carried out at a scanning rate of 0.1 mV s⁻¹ in the voltage range of 2.0–4.0 V (Fig. 4g). It can be seen that the first cycle of O3-Na_{0.67} only shows a pair of main redox peaks assigned to O3–P3 phase transition at 2.6/3.1 V. Comparatively, the traditional P2-Na_{0.67} electrode with 0.67 Na content displays three pairs of additional peaks at 3.35/3.25, 3.65/3.55 and 3.70/3.63 V (Supplementary Fig. 14), which represent Na⁺/vacancy rearrangement in the Na layer upon de/sodiation. The disruption of Na⁺/vacancy order originates from the ionic disorder distribution of the transition metal layer in the high entropy system, and thus facilitates efficient and reversible Na⁺ de/intercalation (Supplementary Fig. 15). The series of characterization confirms the anomalous structure can effectively suppress the Na⁺/vacancy rearrangement, exhibits a stable electrochemical behavior and good electrochemical properties.

The redox mechanism of transition metals is further corroborated by ex situ XAS and XPS results over the electrochemical process. Supplementary Fig. 16 presents the X-ray absorption near-edge structure (XANES) spectra at Ni, Fe, Co, and Mn K-edges. The spectra of these elements all exhibit an obvious shift towards the higher energy region at charging and subsequently move backward upon discharging to 2.0 V, highlighting its multi-redox centers characteristic^{47,48}.

Analysis of XPS spectroscopy evolution in Supplementary Figs. 17–18 further confirms the active redox centers in the forms of Ni^{2+/3+}, Co^{2+/3+}, Fe^{3+/4+}, and Mn^{3+/4+}. Comparatively, no significant spectra shift is observed for Cu and Ti throughout the charging and

discharging cycle (Supplementary Figs. 19–20), suggesting electrochemically inactivity and the structural pillar role of Cu²⁺ and Ti⁴⁺. The binding energy of all elements returns to the original positions at the discharging state, indicating the high reversibility of the redox process. The combination characteristics of multiple redox centers, high redox reversibility, and dual pillar ion promise good cyclic stability.

Further tests, including structural stability, air/water stability, thermal stability, potassium-ion battery and full cell performance, were performed to evaluate the practical application capability of the O3-Na_{0.67} materials. After 100 cycles at 86.5 mA g⁻¹, the O3-Na_{0.67} positive electrode was characterized by XRD, and the pattern was compared with uncycled material to investigate the structural integrity. Although the diffraction peaks of cycled positive electrode slightly shift to the higher angles, the structure still retains a clear O3 phase without any additional phase, indicating good structural reversibility during repeated Na⁺ de-intercalation (Fig. 5a). To test the air stability, the as-prepared sample was aged in a box with a controlled relative humidity of 60% for 18 hours (Exp 18 h) or soaked in deionized water for 12 h (Water 12 h). Figure 5b displays the comparison of XRD results of as-prepared and aged materials. All three samples show a pure O3-type phase without any new peak. Furthermore, air exposure has virtually no effect on electrochemical performance (Supplementary Fig. 21). Water immersion does not lead to significantly decayed electrochemical property (Supplementary Table 22) and only reduces the capacity by 5 mA h g⁻¹, and the cycling stability of soaked sample is even improved (Fig. 5c). To eliminate the effect of Cu element on the stability of air and water, the Cu-free low-sodium O3 material we

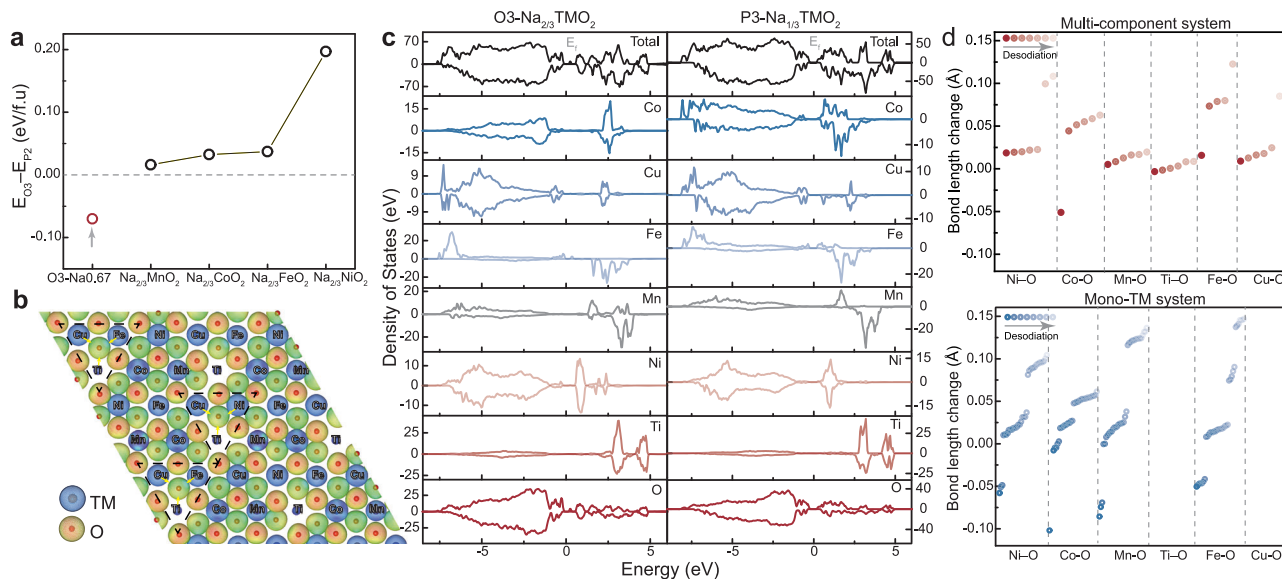


Fig. 6 | DFT insights into phase stability and redox mechanism. **a** The energy difference between the O3 and P2 phases ($E_{O3}-E_{P2}$) for $\text{Na}_{0.67}\text{TMO}_2$ configuration. **b** The ELF calculation results of high-entropy system. **c** The comparative PDOS of

$\text{Na}_{0.67}\text{TMO}_2$ and $\text{Na}_{0.33}\text{TMO}_2$. **d** The bond length change of the TM–O bond upon desodiation in multi-component (red) and the corresponding mono-TM systems (blue).

synthesized also demonstrated an equally comparable stability (Supplementary Fig. 22). A differential scanning calorimetry (DSC) test was conducted on a 4.0 V charged sample to evaluate its thermal stability. The thermal behavior of the positive electrode shows an onset temperature consistent with typical layered oxides, while the measured heat generation of 208.2 J g^{-1} is reduced (Fig. 5d)⁵⁰. In addition, the strategy also presents an opportunity for potassium-ion batteries de/inserting larger charge carrier ions (Fig. 5e). Figure 5f and Supplementary Fig. 23 show the electrochemical performance of K||O3-Na0.67 cells in a voltage range of 1.5–3.9 V at 86.5 mA g^{-1} . Due to the obvious electrostatic repulsion between potassium ions, K^+ generally tends to occupy a larger prismatic position rather than an octahedral space. Consequently, the synthesis of O-type $\text{K}_{1-x}\text{TMO}_2$ layered structures poses significant challenges. O3-KCrO₂ is the only electrochemically active O-type K-ion layered oxide and exhibits multiplatform electrochemical curves and poor cycling stability during de/potassiation^{51,52}. The positive electrode showcases smooth GCD profiles and a good cycling stability of 70.24% capacity retention after 100 cycles. A full cell with O3-Na0.67 as the positive electrode and hard carbon (HC) as the negative electrode was assembled to assess the practical application potential. The cell can show an initial reversible specific capacity of $115.22\text{ mA h g}^{-1}$ and an initial coulombic efficiency of 83.5% cycled within 1.0–4.0 V at 17.3 mA g^{-1} (Fig. 5g), this performance is competitive among recently reported layered oxide cathodes with Na content of 0.67 (Supplementary Table 23). Under cycled at 86.5 mA g^{-1} , the battery maintains a good capacity retention of 83.28% after 150 cycles (Fig. 5h, i), indicating the practicality of the material.

DFT calculations were carried out to gain a deeper understanding of the structural evolution and high stability (The atomic coordinates of the optimized structures are provided in Supplementary Data 1). In the mono-TM systems, the transition metal exhibits a mixed valence state of +3/+4. Given the lack of reported stable electronic configurations for Cu and Ti within a layered oxide structure, mono-TM configurations of other elements (Mn, Co, Fe, and Ni) are used for calculation comparison. The formation energy calculations for $\text{Na}_{0.67}\text{TMO}_2$ configuration indicate that typical mono-TM compounds exhibit the P2 phase with positive $E_{O3}-E_{P2}$ energy, whereas the high-entropy material still maintains the thermodynamically stable O3 phase at 0.67 of Na content (Fig. 6a), consistent with the aforementioned XRD observations. The structural inversion is primarily

attributed to the configurational anisotropy of the transition metal layers within the high-entropy system, as shown in the electronic localization function (ELF) calculation results in Fig. 6b and Supplementary Fig. 24. The disordered ion arrangement originates from diverse transition metal ion components. By reducing the average ionic electronegativity of transition metals, we can enhance the ionicity of TM–O, increase the bond length, and alleviate the lattice distortion caused by the local distortion of ions due to the Jahn-Teller effect. The calculated partial density of states (PDOS) in Fig. 6c further substantiates the multiple redox centers feature in high-entropy material upon the desodiation process from $\text{Na}_{0.67}\text{TMO}_2$ to $\text{Na}_{0.33}\text{TMO}_2$. The vast majority of transition metal elements, namely Ni, Co, Cu, Fe, and Mn, are actively involved in charge compensation, as evidenced by the electronic state variation. The PDOS change for Cu is relatively insignificant, and thus its redox behavior cannot be observed in the experimental spectrum. In contrast, Ti serves as an inactive pillar element to improve structural stability, primarily because the Ti $3d\ t_{2g}$ level located at relatively lower energy and far from the Fermi level is less likely to participate in redox reactions⁵³. We also compare the bond length variations of elements upon desodiation in multi-component and corresponding mono-TM systems, as illustrated in Fig. 6d. For single-component materials, redox centers uniformly distribute throughout the crystal lattice and undergo more consistent local structural variation during charge compensation, which readily leads to substantial structural alterations. Comparatively, the coexistence of 6 TMs in high-entropy materials forms multi-level redox centers. These centers prevent excessive accumulation of local charges through step-based redox reactions, avoid phase transition stress caused by intense voltage jumps of single elements, and enhance the stability of the structure during charging and discharging. Benefiting from the combined effects of structural anisotropy, multiple redox centers, and pillar elements, the local structural changes in high-entropy systems are considerably minimized, contributing a good long-term cycling stability.

Discussion

The stacking structure of the layered oxide is essentially the manifestation of the competition between the electrostatic polarization of AO_2 and TMO_2 layers. In the complex high-entropy systems with diverse components, we proposed the concept of electronegativity entropy weight

W_x to describe the interlayer interactions within high-entropy systems. Here, IEN quantifies the interaction between cations and oxygen electron clouds, while S_{config} characterizes the extent of the impact of entropic disorder on phase structure. By designing systems with a relatively large W_x , we constructed an unusual O3-type structure with the low sodium content of 0.538. Designed unusual materials exhibit different properties from conventional O3 materials, where low sodium content provides improved air stability, and high entropy-induced electron localization imparts good structural stability. The low sodium content creates more alkali metal vacancies, and the high entropy configuration forms a stable framework that facilitates the de-intercalation of large-radius K^+ ions. This different O3 structure makes the material a promising positive electrode candidate for potassium-ion batteries, demonstrating good structural stability. This different structural design represents an effective strategy for exploring potential alkali metal positive electrode materials. Building on the advances in low-sodium O3-phase, we established a computational descriptor for entropy-dominated structures by integrating parameters such as electronegativity difference, ionic radius, configurational entropy, and alkali-to-transition-metal ratio, thereby constructing an O3/P2 phase stability database. This enables neural network-driven prediction of next-generation battery materials candidates, creating a pathway from fundamental descriptor development to large-scale industrial deployment. Furthermore, a deeper understanding of how diverse components determine structural chemistry will provide critical theoretical insights for the future development of high-performance layered positive electrode materials.

Methods

Material synthesis

$\text{Na}_{0.67}\text{Ni}_{0.33}\text{Mn}_{0.67}\text{O}_2$ ($N=2$, P2-Na0.67), $\text{Na}_{0.67}\text{Ni}_{0.18}\text{Cu}_{0.18}\text{Mn}_{0.64}\text{O}_2$ ($N=3$), $\text{Na}_{0.67}\text{Ni}_{0.18}\text{Cu}_{0.18}\text{Co}_{0.15}\text{Mn}_{0.49}\text{O}_2$ ($N=4$), $\text{Na}_{0.67}\text{Ni}_{0.18}\text{Cu}_{0.18}\text{Co}_{0.15}\text{Fe}_{0.15}\text{Mn}_{0.34}\text{O}_2$ ($N=5$), $\text{Na}_{0.67}\text{Ni}_{0.18}\text{Cu}_{0.18}\text{Co}_{0.15}\text{Fe}_{0.15}\text{Mn}_{0.17}\text{Ti}_{0.17}\text{O}_2$ ($N=6$, O3-Na0.67), $\text{Na}_{0.538}\text{Ni}_{0.18}\text{Cu}_{0.18}\text{Co}_{0.15}\text{Fe}_{0.15}\text{Mn}_{0.17}\text{Ti}_{0.17}\text{O}_2$ (O3-Na0.538), $\text{NaNi}_{0.18}\text{Cu}_{0.18}\text{Co}_{0.15}\text{Fe}_{0.15}\text{Mn}_{0.17}\text{Ti}_{0.17}\text{O}_2$ (O3-Na1), $\text{Na}_{0.67}\text{Cu}_{0.18}\text{Co}_{0.15}\text{Fe}_{0.15}\text{Mn}_{0.35}\text{Ti}_{0.17}\text{O}_2$ (No Ni), $\text{Na}_{0.67}\text{Ni}_{0.18}\text{Co}_{0.15}\text{Fe}_{0.15}\text{Mn}_{0.35}\text{Ti}_{0.17}\text{O}_2$ (No Cu), $\text{Na}_{0.67}\text{Ni}_{0.18}\text{Cu}_{0.18}\text{Fe}_{0.15}\text{Mn}_{0.32}\text{Ti}_{0.17}\text{O}_2$ (No Co), $\text{Na}_{0.67}\text{Ni}_{0.18}\text{Cu}_{0.18}\text{Co}_{0.15}\text{Mn}_{0.32}\text{Ti}_{0.17}\text{O}_2$ (No Fe), $\text{Na}_{0.67}\text{Ni}_{0.18}\text{Cu}_{0.18}\text{Co}_{0.15}\text{Fe}_{0.15}\text{Mn}_{0.34}\text{O}_2$ (No Ti), $\text{Na}_{0.67}\text{Ni}_{0.18}\text{Cu}_{0.18}\text{Co}_{0.15}\text{Fe}_{0.15}\text{Ti}_{0.34}\text{O}_2$ (No Mn), $\text{Na}_{0.67}\text{Ni}_{0.18}\text{Cu}_{0.18}\text{Mg}_{0.12}\text{Fe}_{0.1}\text{Mn}_{0.22}\text{Ti}_{0.2}\text{O}_2$ ($N=6_1$), $\text{Na}_{0.67}\text{Ni}_{0.18}\text{Cu}_{0.18}\text{Fe}_{0.15}\text{Co}_{0.15}\text{Mn}_{0.14}\text{Ti}_{0.1}\text{Sn}_{0.1}\text{O}_2$ ($N=7$), $\text{Na}_{0.67}\text{Cu}_{0.15}\text{Mg}_{0.15}\text{Fe}_{0.15}\text{Co}_{0.15}\text{Mn}_{0.1}\text{Ti}_{0.1}\text{Sn}_{0.2}\text{O}_2$ ($N=7_1$), $\text{Na}_{0.67}\text{Ni}_{0.12}\text{Zn}_{0.12}\text{Mg}_{0.12}\text{Fe}_{0.1}\text{Co}_{0.1}\text{Al}_{0.1}\text{Mn}_{0.24}\text{Ti}_{0.1}\text{O}_2$ ($N=8$) and materials of supplementary information were synthesized through a typical solid-state method from stoichiometric amounts of Na_2CO_3 (5 mol% excess, 99.5%, Aladdin), Li_2CO_3 (99%, Aladdin), K_2CO_3 (99%, Aladdin), NiO (98%, Sinopharm Chemical Reagent Co., Ltd), Mn_2O_3 (98%, Aladdin), CuO (99.9%, Aladdin), Co_3O_4 (99.9%, Aladdin), Fe_2O_3 (99.9%, Aladdin), SnO_2 (99.5%, Aladdin), MgO (98.0%, Aladdin) and TiO_2 (99.99%, Aladdin). The powder was pressed into pellets under 16 MPa and heated to 950 °C at a rate of 5 °C per minute, and calcined in air for 12 h (BTF-1200C-4D-4M, Anhui Beyike Equipment Technology Co, Ltd). The samples transfer to the glove box filled with Ar immediately after preparation (H_2O and $\text{O}_2 < 0.1$ ppm).

Hydration tests

The exposed samples were obtained by placing fresh materials in a constant temperature and constant humidity box with a controlled relative humidity (RH) value of 40% under 25 °C in the air. The accurate RH is determined accuracy $\pm 1\%$. The exposed samples were obtained by soaking fresh samples in deionized water for 12 h and then dried in a vacuum drying oven at 80 °C for 12 h.

Materials characterization

The XRD data were acquired by a Persee instrument with Cu K α radiation ($\lambda = 1.5406 \text{ \AA}$) of Rigaku Ultima IV diffractometer. The residual species in the samples was identified by TGA (NETZSCH STA 449F5)

under an Ar atmosphere. Surface information on materials was collected by XPS (ESCALAB 250Xi spectrometer, Thermo Fisher Scientific) with an Al K α achromatic X-ray source. Microstructural information was obtained by scanning electron microscopy (TESCAN MIRA LMS), and HRTEM image were obtained by TEM (JEM 2100 F). The EDS mapping were obtained by TEM (FEI Talos F200X G2). The elemental composition of the materials was analysed through an inductively coupled plasma optical emission spectrometer (Thermo Fisher, ICP-OES). X-ray absorption fine structure (XAFS) spectroscopy was carried out using the Rapid XAFS 2M (Anhui Absorption Spectroscopy Analysis Instrument Co., Ltd.) by fluorescence mode at 20 kV and 30 mA (or 10 kV and 20 mA), and the Si (533) spherically bent crystal analyzer with a radius of curvature of 500 mm was used for Co, the Si (533) spherically bent crystal analyzer with a radius of curvature of 500 mm was used for Cu, the Si (531) spherically bent crystal analyzer with a radius of curvature of 500 mm was used for Fe, the Si (440) spherically bent crystal analyzer with a radius of curvature of 500 mm was used for Mn.

Electrochemical measurements

Coin cells (CR2032) were assembled in an argon-filled glovebox (H_2O and $\text{O}_2 < 0.1$ ppm) for all the electrochemical tests. All electrochemical tests were conducted inside a temperature-controlled climatic chamber maintained at 27 ± 1 °C with convection heating, in ambient air atmosphere. The specific current ($\text{A g}^{-1}/\text{mA g}^{-1}$) and specific capacity (mA h g^{-1}) values reported throughout this work are calculated based on the mass of the active material alone in the positive electrode. The working electrode was prepared by grinding in a mortar with a uniform mixture of active material (80 wt.%), polyvinylidene difluoride (PVDF) (10 wt.%) and Super P carbon (10 wt.%) with N-methyl-pyrrolidone (NMP, $\geq 99.5\%$, Aladdin) as dispersion solvent. The slurry was coated to the surface of aluminum foil by doctor blade in a controlled environment with RH < 30% and used vacuum drying oven at 80 °C for 12 h. The areal loading of the active material was about 2.0–3.5 mg cm^{-2} . The electrodes were cut into circular discs with a diameter of 10 mm by an MTI slicing machine (MSK-T10). The various electrochemical properties of the electrodes were tested by assembling CR2032 by using sodium and potassium pieces as the negative electrode. Sodium ($\geq 99.7\%$, Aladdin) and potassium ($\geq 99\%$, Aladdin) ingots stored in kerosene were first cleared of surface oxidation using a knife. The cleaned metals were rolled into thin sheets (<1 mm thick) using a stainless steel rod and cut into 10 mm diameter circular pieces. For sodium-ion half-cells, the electrolyte is 1 M NaClO_4 (5% by volume of fluoroethylene carbonate (FEC) dissolved in propylene carbonate (supplier DoDoChem), and separator using by porous glass fiber (Whatman, Grade GF/C, No.1822-047) to isolate the direct contact between positive and negative electrodes. Charge–discharge measurements were performed in a voltage range of 2.0–4.0 V (versus Na|Na $^+$) at 86.5 mA g^{-1} after 6 h of relaxation on a LAND (Wuhan, China) battery test system. For the K ion half-cell, the electrolyte solution used in this study was 0.8 M KPF_6 in ethylene carbonate /diethyl carbonate (1:1 by volume, supplier DoDoChem). A typical galvanostatic charge-discharge test was performed in the voltage range of 1.5–3.9 V (versus K|K $^+$) for the half-cell. The hard carbon negative electrode was prepared by grinding in a mortar with a uniform mixture of the hard carbon (Kuraray, 80 wt.%), Super-P carbon black (10 wt.%) and polyacrylic acid (dissolved in water, 10 wt.%). The resultant slurry was uniformly pasted onto Cu foil using the doctor blade method and then carefully dried at 110 °C for 12 h under vacuum. The electrodes were cut into circular discs with a diameter of 12 mm by an MTI slicing machine (MSK-T10). The areal loading of the active material was about 1.4–2.5 mg cm^{-2} . To remove irreversible capacity in the first cycle, the hard carbon negative electrode was recycled in the voltage range of 0.01–2.0 V for three cycles before the full cell was fabricated. Full cell balance was achieved by maintaining the capacity ratio of the negative electrode to the positive electrode (N/P ratio) at 1.2:1. CV experiments

were performed within the same potential range at 0.1 mV s^{-1} . CV was carried out on an Autolab electrochemical workstation in a voltage range of 2.0–4.0 V. For each type of electrochemical experiment, at least three independent coin cells were fabricated and tested to ensure the reproducibility of the results. The charge-discharge curves and performance data presented in the main text figures are from a single, representative cell that exhibited performance closest to the average of all tested cells. The Coulombic efficiency (CE) for each cycle was calculated as the ratio of the discharge capacity to the charge capacity in the preceding charge cycle.

The GITT test were carried out on a Land CT2001A battery test system (Land, Wuhan, China) by CR2032. In the GITT test, the battery was charged/discharged at a current density of 8.65 mA g^{-1} for 15 min and relaxed for 4 h, and the above steps were repeated to reach 4.0/2.0 V. The voltage data were recorded at a sampling rate of 1 point per 20 s. The detailed calculation formula is as follows:

$$D_{\text{Na}^+} = \frac{4}{\pi\tau} \left(\frac{nV_m}{S} \right)^2 \left(\frac{\Delta E_s}{\Delta E_t} \right)^2 \quad (2)$$

This formula is applicable when the working current is very small. The τ represents relaxation time; The n represents moles number of electrode active material; The V_m represents the molar volume of the electrode material; The ΔE_t represents the current charging/discharging voltage variety. The ΔE_s represents the voltage change caused by the pulse; The S represents the contact area of the electrode/electrolyte.

In situ XRD diffraction measurement

The in situ XRD measurements were performed using an opening window cell to allow the X-ray to collect the positive signal on the Al foil collector. The O3-Na0.67 positive electrode and sodium negative electrode were prepared as described in the ‘Electrochemical Measurements’ section. The electrolyte was 1 M NaClO₄ in PC with 5% FEC. A glass fiber separator (Whatman, Grade GF/C, No.1822-047) was used. The cell was assembled in an Ar-filled glovebox ($\text{H}_2\text{O}/\text{O}_2 < 0.1 \text{ ppm}$).

Data availability

The source data generated in this study are provided in the Source Data file. Source data are provided in this paper.

References

- Manthiram, A. A reflection on lithium-ion battery cathode chemistry. *Nat. Commun.* **11**, 1550 (2020).
- Usiskin, R. et al. Fundamentals, status and promise of sodium-based batteries. *Nat. Rev. Mater.* **6**, 1020–1035 (2021).
- Li, M. et al. Unravelling the structure-stability interplay of O3-type layered sodium cathode materials via precision spacing engineering. *Nat. Commun.* **16**, 2010 (2025).
- Chen, S. et al. Challenges and perspectives for NASICON-type electrode materials for advanced sodium-ion batteries. *Adv. Mater.* **29**, 1700431 (2017).
- Li, P. et al. A comprehensive review of layered transition metal oxide cathodes for sodium-ion batteries: The latest advancements and future perspectives. *Mater. Sci. Eng. R Rep.* **163**, 100902 (2025).
- Guo, Y.-J. et al. Sodium layered oxide cathodes: properties, practicality and prospects. *Chem. Soc. Rev.* **53**, 7828–7874 (2024).
- Delmas, C., Fouassier, C. & Hagemuller, P. Structural classification and properties of the layered oxides. *Physica B+C* **99**, 81–85 (1980).
- Keller, M., Buchholz, D. & Passerini, S. Layered Na-ion cathodes with outstanding performance resulting from the synergetic effect of mixed P- and O-type phases. *Adv. Energy Mater.* **6**, 1501555 (2016).
- Fouassier, C., Delmas, C. & Hagemuller, P. Evolution structurale et proprietes physiques des phases $A_x\text{MO}_2$ ($A = \text{Na}, \text{K}; M = \text{Cr}, \text{Mn}, \text{Co}$) ($x \leq 1$). *Mater. Res. Bull.* **10**, 443–449 (1975).
- Hong, F. et al. Phase engineering of Ni-Mn binary layered oxide cathodes for sodium-ion batteries. *J. Energy Chem.* **91**, 501–511 (2024).
- Huang, Y. et al. Negative enthalpy doping stabilizes P2-type oxides cathode for high-performance sodium-ion batteries. *Adv. Mater.* **37**, 2408012 (2025).
- Zhao, C. et al. Rational design of layered oxide materials for sodium-ion batteries. *Science* **370**, 708–711 (2020).
- Cartledge, G. H. Studies on the periodic system. I. The ionic potential as a periodic function. *J. Am. Chem. Soc.* **50**, 2855–2863 (1928).
- Kim, S. C. et al. High-entropy electrolytes for practical lithium metal batteries. *Nat. Energy* **8**, 814–826 (2023).
- Huang, Z. et al. Atomic scale responses of high entropy oxides to redox environments. *Nano Lett.* **24**, 11537–11543 (2024).
- Gao, H. et al. Revealing the potential and challenges of high-entropy layered cathodes for sodium-based energy storage. *Adv. Energy Mater.* **14**, 2304529 (2024).
- Yeh, J. W. et al. Nanostructured high-entropy alloys with multiple principal elements: novel alloy design concepts and outcomes. *Adv. Eng. Mater.* **6**, 299–303 (2004).
- Sun, Y. & Dai, S. High-entropy materials for catalysis: A new frontier. *Sci. Adv.* **7**, eabg1600 (2021).
- Wang, X. et al. Continuous 2000 K droplet-to-particle synthesis. *Mater. Today* **35**, 106–114 (2020).
- Rost, C. M. et al. Entropy-stabilized oxides. *Nat. Commun.* **6**, 8485 (2015).
- Cao, G., Yang, S., Ren, J.-C. & Liu, W. Electronic descriptors for designing high-entropy alloy electrocatalysts by leveraging local chemical environments. *Nat. Commun.* **16**, 1251 (2025).
- Wang, K. et al. Synergy of cations in high entropy oxide lithium ion battery anode. *Nat. Commun.* **14**, 1487 (2023).
- Kuang, J. et al. Charge tuning and anchor effect achieving stable high-voltage layered metal oxides for sodium-ion battery. *Angew. Chem. Int. Ed.* **64**, e202500715.
- Ding, F. et al. Tailoring planar strain for robust structural stability in high-entropy layered sodium oxide cathode materials. *Nat. Energy* **9**, 1529–1539 (2024).
- Zhang, J. et al. Configuration design and interface reconstruction to realize the superior high-rate performance for sodium layered oxide cathodes. *Adv. Energy Mater.* **15**, 2405951 (2025).
- Wang, H. et al. Manipulating local chemistry and coherent structures for high-rate and long-life sodium-ion battery cathodes. *ACS Nano* **18**, 13150–13163 (2024).
- Xiao, J. et al. A hydro-stable and phase-transition-free P2-type cathode with superior cycling stability for high-voltage sodium-ion batteries. *Chem. Eng. J.* **506**, 160010 (2025).
- Wang, H. et al. High-entropy Na-deficient layered oxides for sodium-ion batteries. *ACS Nano* **17**, 12530–12543 (2023).
- Song, J. et al. Entropy stabilization strategy for enhancing the local structural adaptability of Li-rich cathode materials. *Adv. Mater.* **35**, 2208726 (2023).
- Zhang, Y. Electronegativities of elements in valence states and their applications. 1. Electronegativities of elements in valence states. *Inorg. Chem.* **21**, 3886–3889 (1982).
- Pauling, L. *The Nature of the Chemical Bond*, Cornell. Ithaca, New York, 350 (1960).
- Pauling, L. The nature of the chemical bond. IV. The energy of single bonds and the relative electronegativity of atoms. *J. Am. Chem. Soc.* **54**, 3570–3582 (1932).
- Yao, H.-R. et al. Excellent air storage stability of Na-based transition metal oxide cathodes benefiting from enhanced Na–O binding energy. *Energy Stor. Mater.* **54**, 661–667 (2023).
- Zhao, C., Avdeev, M., Chen, L. & Hu, Y.-S. An O3-type oxide with low sodium content as the phase-transition-free anode for sodium-ion batteries. *Angew. Chem. Int. Ed.* **57**, 7056–7060 (2018).

35. Li, K. & Xue, D. Estimation of electronegativity values of elements in different valence states. *J. Phys. Chem. A* **110**, 11332–11337 (2006).
 36. Zheng, W. et al. The promise of high-entropy materials for high-performance rechargeable Li-ion and Na-ion batteries. *Joule* **7**, 2732–2748 (2023).
 37. Kenny, D. S. & Navrotsky, A. Approximate activity-composition relations in the system MgO ZnO at 1205±5 °C. *J. Inorg. Nucl. Chem.* **34**, 2115–2119 (1972).
 38. Takeda, Y. et al. Sodium deintercalation from sodium iron oxide. *Mater. Res. Bull.* **29**, 659–666 (1994).
 39. Yin, C. et al. Structural insights into composition design of Li-rich layered cathode materials for high-energy rechargeable battery. *Mater. Today* **51**, 15–26 (2021).
 40. Wang, P.-F. et al. An ordered Ni₆-ring superstructure enables a highly stable sodium oxide cathode. *Adv. Mater.* **31**, 1903483 (2019).
 41. Wang, P.-F., Yao, H.-R. & Liu, X.-Y. Na⁺/vacancy disordering promises high-rate Na-ion batteries. *Sci. Adv.* **4**, eaar6018 (2018).
 42. Hwang, J.-Y., Kim, J., Yu, T.-Y. & Sun, Y.-K. A new P2-type layered oxide cathode with extremely high energy density for sodium-ion batteries. *Adv. Energy Mater.* **9**, 1803346 (2019).
 43. Yuan, D. et al. P2-type Na_{0.67}Mn_{0.65}Fe_{0.2}Ni_{0.15}O₂ cathode material with high-capacity for sodium-ion battery. *Electrochim. Acta* **116**, 300–305 (2014).
 44. Li, Z.-Y., Gao, R., Sun, L., Hu, Z. & Liu, X. Designing an advanced P2-Na_{0.67}Mn_{0.65}Ni_{0.2}Co_{0.15}O₂ layered cathode material for Na-ion batteries. *J. Mater. Chem.* **3**, 16272–16278 (2015).
 45. Kang, W. et al. P2-Type Na_xCu_{0.15}Ni_{0.20}Mn_{0.65}O₂ cathodes with high voltage for high-power and long-life sodium-ion batteries. *ACS Appl. Mater. Interfaces* **8**, 31661–31668 (2016).
 46. Komaba, S. et al. Study on the reversible electrode reaction of Na_{1-x}Ni_{0.5}Mn_{0.5}O₂ for a rechargeable sodium-ion battery. *Inorg. Chem.* **51**, 6211–6220 (2012).
 47. Cheng, J.-H. et al. Simultaneous reduction of Co³⁺ and Mn⁴⁺ in P2-Na_{2/3}Co_{2/3}Mn_{1/3}O₂ as evidenced by X-ray absorption spectroscopy during electrochemical sodium intercalation. *Chem. Mater.* **26**, 1219–1225 (2014).
 48. Gao, X. et al. Cationic-potential tuned biphasic layered cathodes for stable desodiation/sodiation. *Sci. Bull.* **67**, 1589–1602 (2022).
 49. Peng, B. et al. Unusual site-selective doping in layered cathode strengthens electrostatic cohesion of alkali-metal layer for practicable sodium-ion full cell. *Adv. Mater.* **34**, 2103210 (2022).
 50. Cui, Z., Liu, C., Wang, F. & Manthiram, A. Navigating thermal stability intricacies of high-nickel cathodes for high-energy lithium batteries. *Nat. Energy* **10**, 490–501 (2025).
 51. Kim, H. et al. Stoichiometric Layered Potassium Transition Metal Oxide for Rechargeable Potassium Batteries. *Chem. Mater.* **30**, 6532–6539 (2018).
 52. Xu, Y. et al. Recent advances in rational design for high-performance potassium-ion batteries. *Chem. Soc. Rev.* **53**, 7202–7298 (2024).
 53. Wei, H. et al. A cobalt-free Li(Li_{0.17}Ni_{0.17}Fe_{0.17}Mn_{0.49})O₂ cathode with more oxygen-involving charge compensation for lithium-ion batteries. *ChemSusChem* **12**, 2471–2479 (2019).
- No. 2023J06028) and 21 C Innovation Laboratory, Contemporary Amperex Technology Ltd. The authors are thankful to the Beijing Synchrotron Radiation Facility for providing support with XAS characterizations at station 1W1B.

Author contributions

Y.G.G., C.Y.O.Y. and H.R.Y. directed the research projects and supervised the work. L.G. synthesized the materials, conducted electrochemical and material characterization measurements, and analyzed the data. F.Z. set up the XAS experiment, L.G. carried out and performed data analysis under the guidance of F.Z. X.G.Y. conducted TEM, SEM, and in situ XRD measurements, and discussed and analyzed the results with L.G. H.R.Y., W.H.H., Y.J.G. and L.G. discussed the principle of electronegativity and the weighting formula, and L.G. performed data statistics on medium/high entropy materials. L.G. set up the air stability test, Q.L.Z., M.W. and W.W.Y. conducted experiments and electrochemical measurements. F.H.N., J.L.L., J.W.D., Z.F.L., J.M.X., Z.Y. and H.R.Y. completed the DFT and machine learning experiments, carried out analysis and discussion. M.L., Y.J.G., D.L.C., L.T.Z. and Z.G.H. discussed the rationality of the experimental results and helped revise the manuscript. L.G. and H.R.Y. wrote the manuscript with input from all co-authors. All authors commented on and reviewed the manuscript.

Competing interests

The authors declare no competing interests.

Additional information

Supplementary information The online version contains supplementary material available at <https://doi.org/10.1038/s41467-025-68016-5>.

Correspondence and requests for materials should be addressed to Hu-Rong Yao, Chuying OuYang or Yu-Guo Guo.

Peer review information *Nature Communications* thanks Hao Liu, Guoxiu Wang and the other anonymous reviewer(s) for their contribution to the peer review of this work. A peer review file is available.

Reprints and permissions information is available at <http://www.nature.com/reprints>

Publisher's note Springer Nature remains neutral with regard to jurisdictional claims in published maps and institutional affiliations.

Open Access This article is licensed under a Creative Commons Attribution-NonCommercial-NoDerivatives 4.0 International License, which permits any non-commercial use, sharing, distribution and reproduction in any medium or format, as long as you give appropriate credit to the original author(s) and the source, provide a link to the Creative Commons licence, and indicate if you modified the licensed material. You do not have permission under this licence to share adapted material derived from this article or parts of it. The images or other third party material in this article are included in the article's Creative Commons licence, unless indicated otherwise in a credit line to the material. If material is not included in the article's Creative Commons licence and your intended use is not permitted by statutory regulation or exceeds the permitted use, you will need to obtain permission directly from the copyright holder. To view a copy of this licence, visit <http://creativecommons.org/licenses/by-nc-nd/4.0/>.

© The Author(s) 2026

Acknowledgements

Y.G.G. discloses support for the research of this work from the Basic Science Center Project of the National Natural Science Foundation of China (Grant No. 52388201). H.R.Y. discloses support for publication of this work from the National Natural Science Foundation of China (Grant No. 22179021), the Natural Science Foundation of Fujian Province (Grant